solids

MDPI

Article

Kinetics of γ-$LiAlO_2$ Formation out of Li_2O-Al_2O_3 Melt—A Molecular Dynamics-Informed Non-Equilibrium Thermodynamic Study

Sanchita Chakrabarty [1], Danilo Alencar De Abreu [2], Iyad Alabd Alhafez [3], Olga Fabrichnaya [2], Nina Merkert [3], Alena Schnickmann [4], Thomas Schirmer [4], Ursula E. A. Fittschen [5] and Michael Fischlschweiger [1,*]

[1] Chair of Technical Thermodynamics and Energy Efficient Material Treatment, Institute of Energy Process Engineering and Fuel Technology, Clausthal University of Technology, Agricolastraße 4, 38678 Clausthal-Zellerfeld, Germany; sanchita.chakrabarty@tu-clausthal.de
[2] Institute of Materials Science, TU Bergakademie Freiberg, Gustav-Zeuner Straße 5, 09599 Freiberg, Germany; danilo-alencar.de-abreu@iww.tu-freiberg.de (D.A.D.A.); olga.fabrichnaya@iww.tu-freiberg.de (O.F.)
[3] Institute of Applied Mechanics, Clausthal University of Technology, Arnold-Sommerfeld-Straße 6, 38678 Clausthal-Zellerfeld, Germany; iyad.alabd.alhafez@tu-clausthal.de (I.A.A.); nina.merkert@tu-clausthal.de (N.M.)
[4] Institute of Disposal Research, Clausthal University of Technology, Adolph-Roemer-Straße 2A, 38678 Clausthal-Zellerfeld, Germany; alena.schnickmann@tu-clausthal.de (A.S.); thomas.schirmer@tu-clausthal.de (T.S.)
[5] Institute of Inorganic and Analytical Chemistry, Clausthal University of Technology, Arnold-Sommerfeld-Straße 4, 38678 Clausthal-Zellerfeld, Germany; ursula.fittschen@tu-clausthal.de
* Correspondence: michael.fischlschweiger@tu-clausthal.de

Abstract: Slags generated from pyrometallurgical processing of spent Li-ion batteries are reservoirs of Li compounds that, on recycling, can reintegrate Li into the material stream. In this context, γ-$LiAlO_2$ is a promising candidate that potentially increases recycling efficiency due to its high Li content and favorable morphology for separation. However, its solidification kinetics depends on melt compositions and cooling strategies. The Engineered Artificial Minerals approach aims to optimize process conditions that maximize the desired solid phases. To realize this goal, understanding the coupled influence of external cooling kinetics and internal kinetics of solid/liquid interface migration and mass and thermal diffusion on solidification is critical. In this work, the solidification of γ-$LiAlO_2$ from a Li_2O-Al_2O_3 melt is computationally investigated by applying a non-equilibrium thermodynamic model to understand the influence of varying processing conditions on crystallization kinetics. A strategy is illustrated that allows the effective utilization of thermodynamic information obtained by the CALPHAD approach and molecular dynamics-generated diffusion coefficients to simulate kinetic-dependent solidification. Model calculations revealed that melts with compositions close to γ-$LiAlO_2$ remain comparatively unaffected by the external heat extraction strategies due to rapid internal kinetic processes. Kinetic limitations, especially diffusion, become significant for high cooling rates as the melt composition deviates from the stoichiometric compound.

Keywords: non-equilibrium thermodynamic model; engineering artificial minerals (EnAM); Li recycling; γ-$LiAlO_2$; phase transformation; controlled solidification

Citation: Chakrabarty, S.; De Abreu, D.A.; Alhafez, I.A.; Fabrichnaya, O.; Merkert, N.; Schnickmann, A.; Schirmer, T.; Fittschen, U.E.A.; Fischlschweiger, M. Kinetics of γ-$LiAlO_2$ Formation out of Li_2O-Al_2O_3 Melt—A Molecular Dynamics-Informed Non-Equilibrium Thermodynamic Study. *Solids* **2024**, *5*, 561–579. https://doi.org/10.3390/solids5040038

Academic Editor: Sophie Guillemet-Fritsch

Received: 30 September 2024
Revised: 4 November 2024
Accepted: 6 November 2024
Published: 12 November 2024

1. Introduction

The study of slag solidification is garnering increasing focus from the scientific community, as resource efficiency and sustainability are becoming integral for technological advancement [1,2]. The humungous quantity of slag that is produced from various pyrometallurgical processes [3,4] has been traditionally treated as waste streams and discarded as landfills or utilized in low-value applications such as cement manufacturing [5–8]. On

the one hand, such an approach could pose potential environmental pollution in terms of groundwater contamination or ecological imbalance due to its hazardous content, such as Cr [9–11]. On the other hand, the potential to reintegrate valuable elements like Li, Ta, Ti, Ni, and Ce from the slag into the material stream that promotes both circular economy and higher economic returns is lost [12–18]. Irrespective of this, further processing of slag is most often not pursued because of the technical complexity and its associated cost of separating out the element of interest from the complex matrix of mineral phases in which the element is distributed in the solidified slag [19–21]. Engineered Artificial Minerals (EnAMs) specifically address this issue with an approach wherein slag solidification can be tailored either via compositional modification or with a controlled cooling strategy, such that the maximized generation of those mineral phases that constitute the highest concentration of the element of interest and are separable from the slag matrix is achieved [22,23].

In this regard, Li-bearing slags, with the critical element Li [24–27] being distributed in dilute proportions into several complex oxide and oxidic solutions [28,29], demand special focus [30]. Previous research work has identified lithium aluminate (γ-$LiAlO_2$) as a promising EnAM phase, as it has a high Li content and favorable morphology for downstream separation processes [30,31]. It must be mentioned here that theoretical calculation identifies the γ form to be the high-temperature polymorph of $LiAlO_2$ that transforms at temperatures below 900 °C into the α form. However, experimentally, such a transformation could hardly be observed, possibly due to extremely slow kinetics [32]. Hence, for most practical purposes in the context of slag valorization, $LiAlO_2$ formation refers to its γ polymorph [33]. This material can be treated as a Li reservoir for further processing to other lithium compounds or can be directly used in a multitude of fields, such as in batteries as electrolyte composites, as an electrolyte matrix material for carbonate fuel cells, in tritium breeder blankets of nuclear reactors for producing tritium, in radiation dosimetry, etc. [34–37]. Hence, it would be worthwhile to investigate the influence of solidification conditions in terms of the slag composition and implemented cooling regimes on the generation of γ-$LiAlO_2$. Experimental investigations on the presence of manganese in suppressing γ-$LiAlO_2$ formation due to the entrapment of Li and Al in manganese-rich spinel solid solutions are found in the literature [38]. Both the promotion and suppression of γ-$LiAlO_2$ in the dependence of the relative ratio of Mg and Ca oxides have been observed [28]. However, the experimental determination of the effect of the coupled and sometimes interdependent process parameters on phase generation is both cost- and time-intensive. This necessitates solidification simulation to elucidate the structure–process–property relation for the entire spectrum of solidification conditions. The CALPHAD approach (Calculation of Phase Diagrams) has been quite successfully and extensively developed and applied to study slag solidification in terms of determining the most stable phases under certain conditions of temperature, pressure, and bulk composition of the system applying the Gibbs energy minimization technique [26,28,39,40]. However, for industry-relevant processing conditions that could deviate substantially from equilibrium [41], the qualitative and quantitative nature of the solidified phases are further influenced by diffusion and/or reaction kinetics that, in turn, are dependent on external cooling rates and the composition domain [42,43]. Such effects have been exemplified in [44], where morphological variations of γ-$LiAlO_2$ that are crucial for downstream separation result from thermal diffusion generated from temperature gradients in the Li-containing slag. In our previous work, the dependence of the solidification rate of Li_2SiO_3 from a Li_2O-SiO_2 melt on external cooling rates could also be demonstrated [45]. Numerous literature data for other melt systems can be cited where the suppression of equilibrium phases or control over their proportions and microstructures is achieved through manipulating the kinetics [46–48]. Non-equilibrium frameworks need to be further developed to account for these kinetic effects and model the deviation from equilibrium behavior. One well-known possibility is the Scheil–Gulliver approach, which considers limited solid diffusion. However, its assumptions of infinite liquid diffusivity and instantaneous solid/liquid interface mobility might not be applicable for slags with high viscosity and precipitating complex solid phases, respectively [49,50].

The non-equilibrium framework based on the thermodynamic extremal principle (TEP) and developed by Svoboda et al. constitutes a thermodynamically consistent interrelation between mixed kinetics (diffusion, solid/liquid interface mobility) and phase transformations [51,52]. Anchored in the maximization of the entropy production principle, TEP circumvents the need for a high degree of idealization of the system and thus holds the physical nature of the problem to an appreciable extent [51]. Although its application for capturing phase evolution kinetics in alloy systems is extensive [53–55], there are relatively fewer investigations of phase transformations in oxidic systems, and they are recent [56]. In our previous works, the isothermal TEP methodology was successfully extended to consider external and internal thermal gradients and implemented to capture the solid–solid and solid–liquid phase transition kinetics on the MgO-Al_2O_3 [57] and Li_2O-SiO_2 systems [45,58].

In this paper, the non-isothermal TEP has been applied to investigate the growth kinetics of γ-$LiAlO_2$ from a binary melt of Li_2O-Al_2O_3. The fundamental understanding of the prevailing mechanisms governing the oxidic solidification of this binary system and its dependence on external process parameters can be extended to higher-order oxidic melts from battery recycling [23,28]. This aids in designing cooling strategies and operational composition domains that tailor the internal melt kinetics to generate non-equilibrium solid-phase characteristics such that the desired element recovery can be achieved.

One important aspect in terms of simulating solidification with TEP-based non-equilibrium models is the determination of kinetic parameters. Herein, kinetic coefficients are predicted with molecular dynamics (MD) simulation [59], which is an alternative strategy to the inverse determination of kinetic parameters, particularly diffusion, based on mathematical optimization and kinetic experiments. This might create the foundation to be less dependent on experiments, particularly for higher-order systems. Furthermore, the fundamental driving forces prevailing in the binary melt and necessary for characterizing the non-equilibrium fluxes governing γ-$LiAlO_2$ solidification have been successfully derived from the Gibbs energies of the Li_2O-Al_2O_3 database recently optimized within the state-of-the-art CALPHAD technology approach [60]. Finally, the non-equilibrium framework of TEP couples the kinetic information of MD with that of the equilibrium thermodynamics of CALPHAD to investigate the solidification kinetics of γ-$LiAlO_2$ from the binary Li_2O-Al_2O_3 melt.

2. Materials and Methods

The non-equilibrium solidification of γ-$LiAlO_2$ from a binary melt containing Li_2O-Al_2O_3 has been investigated in this work considering the mixed internal kinetics of solid/liquid interface migration and mass and thermal diffusion in the dependence on external kinetics, such as varying cooling strategies. In this section, firstly, the physical model is briefly introduced, wherein the characteristic variables of the system are described. Following this, the major TEP equations that govern the temporal evolution of these variables, which are key to characterizing kinetic solidification, are presented. Finally, the simultaneous connection between the kinetic TEP model with the equilibrium-based CALPHAD information and MD simulation information is described.

2.1. Schematic Explanation and Representation of the Solidification System

A 1D crystallization evolution of the γ-$LiAlO_2$ phase from the binary Li_2O-Al_2O_3 melt system has been schematically represented in Figure 1. A sharp planar solid/liquid interface that has been reported as characteristic of oxide systems [61] has been considered in this work. An initial nucleation of the solid phase on one boundary of the system has been considered such that the present solidification study could be focused on the growth kinetics of the existing solid/liquid interface. Three different melt compositions with the molar ratio of Li_2O-Al_2O_3 as 0.55:0.45, 0.6:0.4, and 0.65:0.35 and that generate γ-$LiAlO_2$ based on thermodynamic equilibrium considerations [60] have been chosen for this study. In the presence of an external sufficiently high cooling rate, multiple kinetic processes

occur simultaneously to propagate solidification. The generation of the solid γ-$LiAlO_2$ phase requires the incorporation of Li_2O and Al_2O_3 from the melt to the solid phase, causing the solid/liquid interface migration with a velocity v into the melt, as has been schematically represented in Figure 1. The mobility of the interface, or the incorporation rate of the components into the solid phase, needs to be infinitely fast for the progression of solidification when the assumption of equilibrium or no driving force is considered, as in most reported solidification models [49,50]. However, the TEP model allows for relaxing such constraints and can deal with a finite interface mobility and, consequently, non-equilibrium interface conditions [52,62].

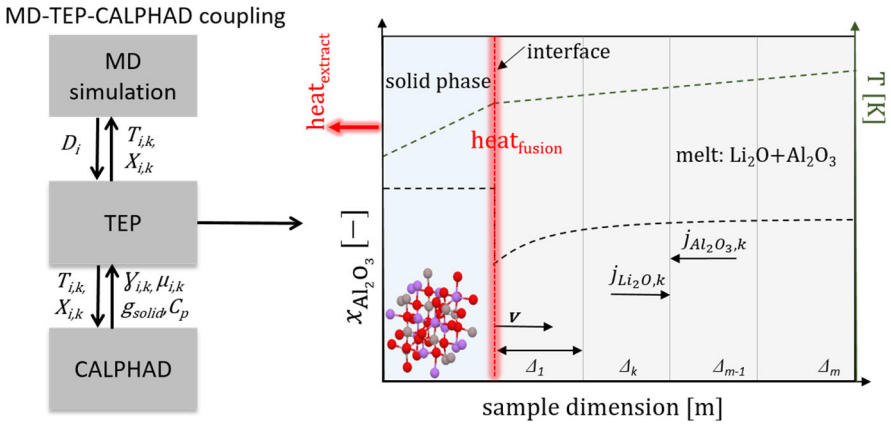

Figure 1. Schematic representation of the material flow between MD-TEP-CALPHAD and the 1D γ-$LiAlO_2$ crystallization system from Li_2O-Al_2O_3 melt. The representative solid structure is computed based on reference [63]. The temperature and composition profiles for a certain time are depicted when the system has been subjected to external heat extraction. The solid/liquid interface moves with velocity v along with a generation of latent heat at the interface.

The combined effect of external heat extraction and the latent heat evolution at the interface during solidification gives rise to the inhomogeneity of the temperature field with time due to the thermophysical properties of the solid-melt system. This is depicted in Figure 1.

Finally, the formation of the stoichiometric compound γ-$LiAlO_2$ with a mole composition of 0.5:0.5 Li_2O-Al_2O_3 from a melt with an Al_2O_3 concentration less than 0.5 requires the diffusion of Al_2O_3 from the bulk toward the interface and that of the Li_2O in the reverse direction. The same is depicted in Figure 1, where the melt has been discretized into k elements of thickness Δ_k. Each region experiences a net positive flux of Li_2O, $j_{i,k}$ (i = Li_2O) and a net negative flux of Al_2O_3. The resulting spatial heterogeneous concentration field for a particular time is shown for the melt in Figure 1. The solid composition is fixed at 0.5.

The evolving interface conditions of temperature and composition are key for determining solidification kinetics.

Before discussing the information flow between the TEP, CALPHAD, and MD simulation, as has been represented in Figure 1, the TEP evolution equations are introduced briefly for the sake of demonstrating the coupling with CALPHAD and MD. For deeper insight into TEP, the reader is referred to [51,62].

2.2. Thermodynamic Extremal Principle (TEP): Evolution Equations

The kinetic processes of mass flux and interface migration, as were discussed in the previous subsection, progress by dissipating the Gibbs energy of the system. Hence, the first step for the TEP framework, as was developed by Svoboda et al. [51,62] for an isothermal system, is the formulation of the rate of Gibbs energy change of the system, $\dot{G}$, in terms of the kinetic variables j_{ik} and v, characterizing the kinetic processes, as is given

in Equations (1) and (2). Readers are referred to [62] for a detailed explanation of firstly representing the total Gibbs energy of the system as a function of j_{ik} and v and consequently deriving the following partial differential equations:

$$\frac{\partial \dot{G}}{\partial j_{ik}} = (\mu_{ik+1} - \mu_{sk+1}) - (\mu_{ik} - \mu_{sk}) \qquad i = 1, \ldots \mathrm{s}-1, k = 1, \ldots \mathrm{m}-1 \tag{1}$$

In Equation (1), s represents the number of components, and m represents the number of discretization in the liquid (since no mass diffusion is considered inside the solid). The chemical potential of the ith component in the kth discretization is denoted by μ_{ik}.

$$\frac{\partial \dot{G}}{\partial v} = \frac{1}{\Omega}\left(g^{solid} - \sum_{i=1}^{s} x_i^{solid}\mu_{i,int}^{liq}\right) \tag{2}$$

In Equation (2), Ω represents the partial molar volume of the components, and g^{solid} represents the Gibbs energy of the solid phase. To represent a value at the interface 'int' on the liquid 'liq' side, the property values for the first discretization are used.

The next step in the TEP methodology is the formulation of a dissipation function Q by considering a linear relation between fluxes and forces, prevalent for the kinetic processes occurring in the system. The partial differential of this function with respect to the kinetic variables is depicted in Equations (3) and (4) according to [51,62].

$$\frac{\partial Q}{\partial j_{ik}} = \frac{2j_{ik}}{B_{ik}} - \frac{2j_{sk}}{B_{sk}} \quad i = 1, \ldots \mathrm{s}-1, k = 1, \ldots \mathrm{m}-1 \tag{3}$$

Here, $B_{ik} = \frac{1}{U_{ik}+U_{ik+1}}$; and $U_{ik} = \frac{RT\Omega\Delta_k}{2x_{ik}D_{ik}}$. D_{ik} represents the diffusion coefficient of the ith component in the kth element. R is the universal gas constant, and T is the system temperature.

Equation (4) is stated as follows:

$$\frac{\partial Q}{\partial v} = \frac{2v}{M} + 2\sum_{i=1}^{s} C_i K_i v \tag{4}$$

where $C_i = K_i U_{i,int}$; $K_i = \frac{x_i^{solid} - x_{i,int}^{liq}}{\Omega}$; and M is the interface mobility.

Finally, undertaking the constrained maximization of Q in terms of the kinetic variables by implementing the maximum entropy production principle, the following relation between $\dot{G}$ and Q is derived [51,62]:

$$\frac{\partial \dot{G}}{\partial \dot{q_l}} = -\frac{1}{2}\frac{\partial Q}{\partial \dot{q_l}} \; l = 1, \ldots, (\mathrm{s}-1)(\mathrm{m}-1)+1 \tag{5}$$

In Equation (5), $\dot{q_l}$ denotes the kinetic variables j_{ik} and v.

Substituting Equations (1) and (3) in Equation (5) generates flux equations related to diffusion. Similarly, substituting Equations (2) and (4) in Equation (5) provides the equation for the interface velocity. The set of linear Equation (5) could then be solved for each time interval to calculate the temporal evolution of the kinetic variables and, consequently, the system. For a more detailed description of TEP, the readers are referred to [51,62].

The above-detailed isothermal TEP framework has been successfully extended to incorporate temporal and spatial temperature inhomogeneity in our previous works [57,58]. As has been discussed in [58], the effect of thermal diffusion due to the presence of a spatio-temporal thermal gradient on the evolution of the kinetic variables could be fully

accounted for [64] by simultaneously solving the 1D heat conduction equation, as is given in Equation (6) [65].

$$\frac{\partial T}{\partial t} = \alpha \frac{\partial^2 T}{\partial z^2} + \frac{\dot{H}}{\rho c_p} \quad (6)$$

Equation (6) is implemented for each discretization z to evaluate the temperature T evolution over time t. It should be mentioned here that the discretization also includes the solid phase in this case, unlike in the case of mass flux, where only the liquid phase was considered (Equations (1) and (3)). $\dot{H}$ represents the heat generation rate by unit volume. This value is zero except for the discretization that includes the interface that acts as a moving heat source during solidification. $\dot{H}$ could be calculated from the information of the experimentally obtained latent heat of fusion for γ-$LiAlO_2$ as can be derived from the literature [66] and the amount of phase generated or the interface velocity information v delivered from TEP. The thermal diffusivity α is represented by $\frac{k}{\rho c_p}$, where k is the thermal conductivity, ρ is the density, and c_p is the specific heat capacity. The α value of pure γ-$LiAlO_2$ was set based on Ref. [67], and for the melt, its value was set based on Refs. [68,69]. The herein applied values for the solid and melt thermal diffusivities are 1.65×10^{-7} m^2s^{-1} and 8.25×10^{-8} m^2s^{-1}, respectively.

The remaining parameters from Equations (1)–(6) are derived from either the CALPHAD database or from MD simulations, as described in the following subsections.

2.3. CALPHAD

The CALPHAD (Calculation of Phase Diagrams) methodology finds widespread application in material science as the tool to study phase formations under equilibrium conditions. Different physically motivated models are implemented to describe the dependence of Gibbs energy on temperature, pressure, and composition for each phase that can form in the system. The thermodynamic parameters describing the dependence of Gibbs energy are obtained from available experimental data, both on phase equilibria and thermodynamic values, by optimization in order to reproduce experimental data within minimal deviation [70]. The resulting thermodynamic parameters could be utilized to calculate Gibbs energies of different phases as a function of pressure, temperature, and composition that could further be used to generate phase equilibrium diagrams [60].

Phase equilibria in the Li_2O-Al_2O_3 system were recently experimentally investigated in depth, and thermodynamic parameters were optimized [60]. In this new assessment, the stability of $LiAlO_2$ was confirmed. The high-temperature polymorph γ-$LiAlO_2$ was modeled as a stoichiometric compound. The liquid phase was described by a two-sublattice partially ionic liquid model. This database provides the g^{solid} and the μ_{ik} values required in Equations (1) and (2) when it receives the conditions of composition x_{ik} and temperature T_{ik} from the TEP framework. The connection procedure between the kinetic model and the equilibrium database has been described in more detail in our previous work [57]. The information flow between TEP and CALPHAD has been schematically represented in Figure 1. The c_p values of the solid and liquid phases required in Equation (6) could also be obtained from the CALPHAD database.

2.4. Molecular Dynamic (MD) Simulation

One of the characteristic variables of the TEP model is the flux of the components Li_2O and Al_2O_3. This implies that diffusion within the melt needs to be described with respect to these oxide species. Herein, the diffusion of the neutral oxide molecules is set as an assumption that satisfies the local charge neutrality constraint on one hand and facilitates feasible computation without the knowledge of the actual diffusion mechanism on the other [71]. Additionally, for each of the oxide molecules, the self-diffusion could be equated to the slower-diffusing constituent ion [72]. However, the experimental determination of such ionic diffusivity is challenging. Hence, it is essential to resort to theoretical calculations to access such information [73].

For the Li_2O-Al_2O_3 system, recent investigation with molecular dynamic simulation with the open-source LAMMPS code [74] could generate the diffusivities of the Li^+, Al^{3+}, and O^{2-} species in the dependence of temperature and composition. The mean square displacement for each ion of each species was computed and then averaged to generate the self-diffusion coefficient D_s of each ionic species according to Equation (7) [59].

$$D_s = \frac{1}{6tN_{ion}} \sum_{i=1}^{N_{ion}} \left[|r_i(t) - r_i(0)|^2 \right] \quad (7)$$

In Equation (7), r_i represents the position of the ion after time t, while N_{ion} represents the total number of ions.

Following the above procedure, the diffusion coefficients for the Li^+, Al^{3+}, and O^{2-} ions that could be generated for different combinations of temperature and composition [59] and further interpolated points have been represented in Figure 2. It must be mentioned that the variation of the diffusion coefficient as a function of composition refers to the self-diffusion coefficients of individual ions for different systems having varied overall mole fraction ratios of Li_2O and Al_2O_3. As can be observed from Figure 2, for most of the combinations of temperature and composition, the Li^+ ion shows the highest diffusivity, followed by that of the O^{2-} and Al^{3+} ions, respectively. Hence, assuming the aspect of charge neutrality constraint, the MD-generated self-diffusion coefficients could be arguably recalculated for the components Li_2O and Al_2O_3 and hence transformed into effective diffusion coefficients D for the oxide molecules required for the TEP framework.

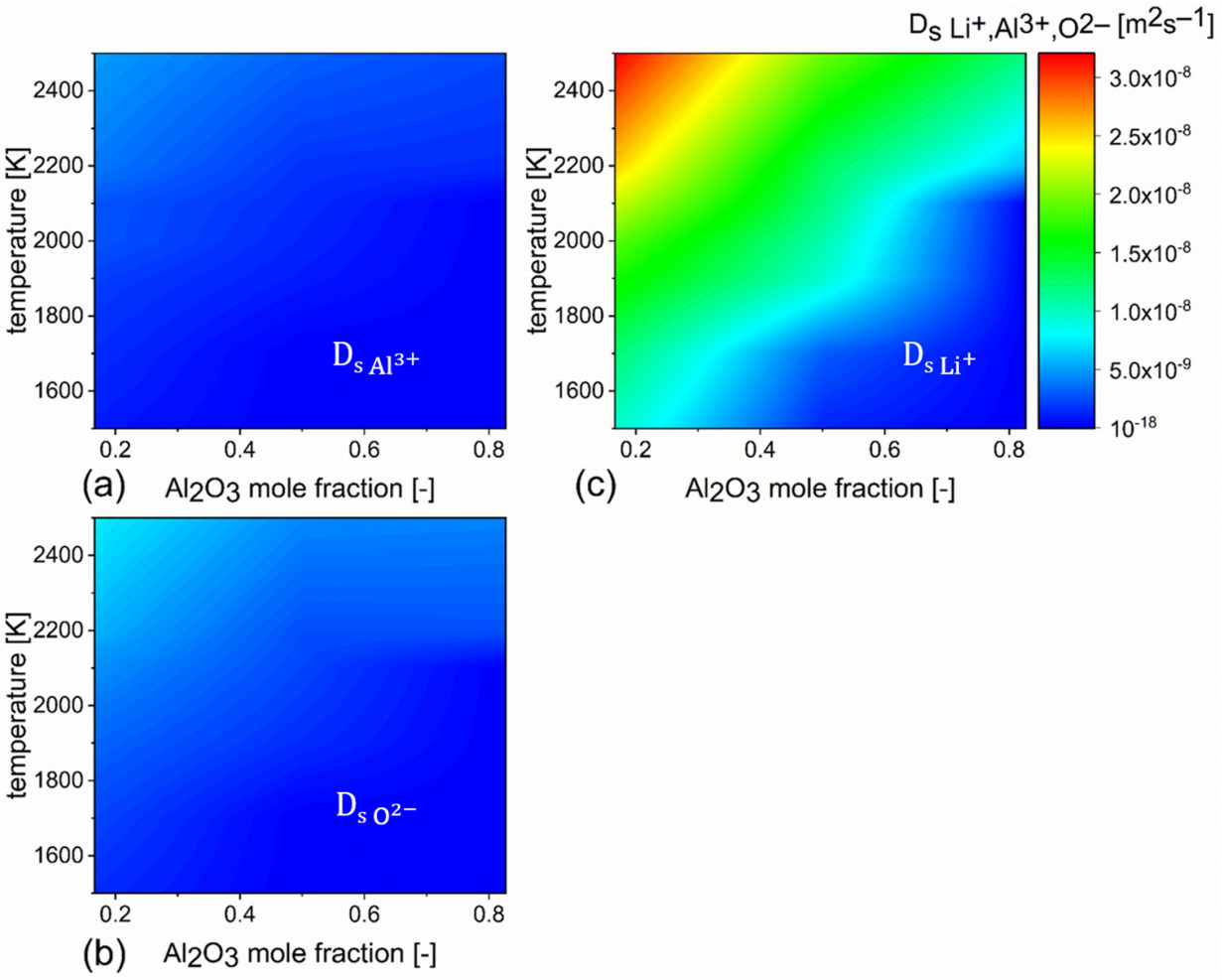

Figure 2. The MD diffusion coefficients of (**a**) Al^{3+}, (**b**) O^{2-}, and (**c**) Li^+ as a function of temperature and composition for a Li_2O-Al_2O_3 binary system.

Finally, these transformed diffusion coefficients could be accessed with regard to the dependence on temperature and composition by the TEP model for solving the fluxes within the melt phase.

Thus, the information flow between CALPHAD-TEP-MD needs to be established at each time step for the successful solution of TEP evolution equations for describing the kinetic solidification of γ-$LiAlO_2$ from a Li_2O-Al_2O_3 binary melt.

3. Results

The TEP modeling framework has been applied in this work to study the solidification kinetics of γ-$LiAlO_2$ from a Li_2O-Al_2O_3 melt. The growth of crystalline Li_2O-Al_2O_3 has been studied with regard to the dependence on external cooling strategies and initial melt composition for a system of dimension 6 mm. Three molar ratios of Li_2O-Al_2O_3, namely, 0.55:0.45, 0.6:0.4, and 0.65:0.35, have been considered for the starting melt composition. For convenience, they have been referred to as C1, C2, and C3 in the subsequent discussion. An initial nucleation of γ-$LiAlO_2$ is assumed. Corresponding to the kinetic processes of mass and thermal diffusion, the kinetic parameters D and α are obtained based on the MD simulations and literature, respectively, as has been discussed in the previous section. Utilizing the experimental finding from [60] that the reaction kinetics of γ-$LiAlO_2$ is quite fast, corresponding to a melt of the same composition, it is assumed in this work that the Gibbs energy dissipation for interface migration is comparably low compared to diffusion. Hence, it is not the rate-limiting factor for solidification in this case and is not considered in this work.

3.1. γ-$LiAlO_2$ Phase Evolution Computationally Investigated for the Cooling Rates 2 Kmin^{-1}, 10 Kmin^{-1}, 40 Kmin^{-1}, 60 Kmin^{-1}, and 100 Kmin^{-1} for Each of the Binary Melts, C1, C2, and C3

For all the simulation cases, the initial melt composition and temperature are considered to be spatially homogeneous. The melt is considered to be cooled from the corresponding liquidus temperatures of the different melts [60] with different cooling rates at the left system boundary (Figure 1). The cooling regime is continued until the left system boundary temperature reaches 1750 K. The right system boundary (Figure 1) is considered to be at adiabatic conditions throughout the process. In Figure 3a, the black, blue, olive, brown, and red solid lines represent the evolution of the left boundary temperature with time for the cooling rates 2 Kmin^{-1}, 10 Kmin^{-1}, 40 Kmin^{-1}, 60 Kmin$^{-1,}$ and 100 Kmin^{-1}, respectively.

The equilibrium mole fraction of crystalline γ-$LiAlO_2$, solidified on cooling melt C1, has been represented as a function of temperature by the black dash line in Figure 3b. The influence of the different boundary cooling rates of 2 Kmin^{-1}, 10 Kmin^{-1}, 40 Kmin^{-1}, 60 Kmin$^{-1,}$ and 100 Kmin^{-1} on the solid-phase evolution has been further depicted by the black, blue, green, brown, and red solid lines, respectively. It must be mentioned here that the temperature axes represent only the temperature at the left boundary. Due to the time-dependent process of thermal diffusion, the spatial temperature distribution for the remaining melt for a certain left boundary temperature value varies according to the cooling rate applied. This is further illustrated in the following results.

As can be observed, the amount of solidified phase fraction approaches the equilibrium value as the cooling rate is reduced. The mole fraction evolution is ~98% of the equilibrium value for both the cooling rates 2 Kmin^{-1} and 10 Kmin^{-1}. It decreased to 96% and 94% of the equilibrium fraction as the cooling rate was increased to 40 Kmin^{-1} and 60 Kmin^{-1}. A comparatively stronger influence on the phase evolution could be observed only when the cooling rate was increased to 100 Kmin^{-1}. However, even for this case, the solid γ-$LiAlO_2$ phase reached a value of about 91% of its equilibrium value.

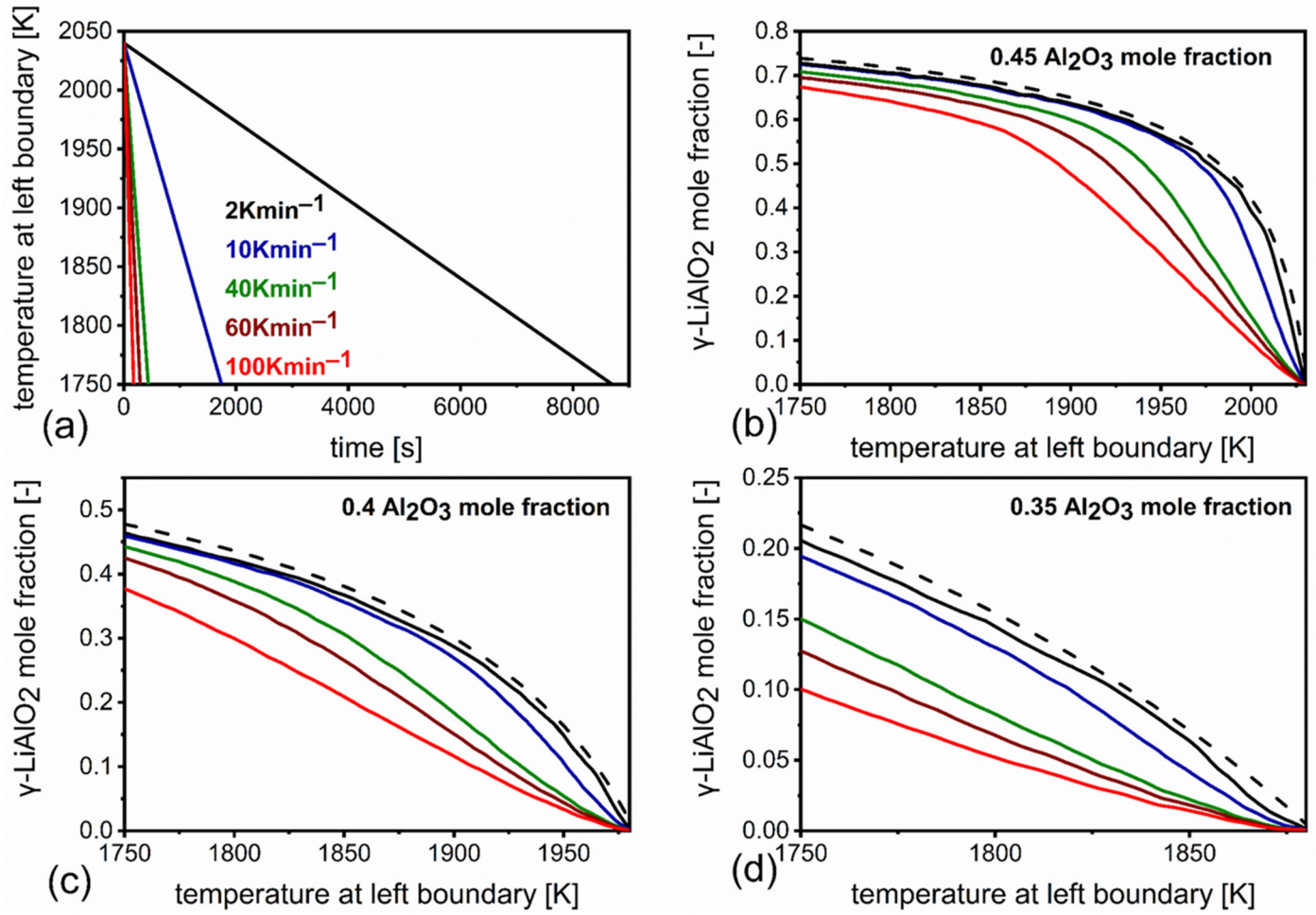

Figure 3. (**a**) Left boundary temperatures over time represented by the black, blue, olive, brown, and red solid lines for the cooling rates 2 Kmin^{-1}, 10 Kmin^{-1}, 40 Kmin^{-1}, 60 Kmin^{-1}, and 100 Kmin^{-1}, respectively; (**b**) solid-phase fraction evolution as a function of left boundary temperature for melt with starting composition C1 (0.45 Al_3) for different cooling rates represented by the corresponding colored solid lines corresponding to the respective cooling rate; (**c**) solid-phase fraction evolution as a function of left boundary temperature for melt with starting composition C2 (0.4 Al_2O_3); (**d**) solid-phase fraction evolution as a function of left boundary temperature for melt with starting composition C3 (0.35 Al_2O_3); for all the cases in (**b**–**d**), the black dash lines represent the equilibrium solid fraction evolution over temperature for the corresponding starting melt compositions.

Similar model calculations for the same cooling rates were performed for C2 and C3 and are represented in Figure 3c,d. The corresponding equilibrium mole fractions are depicted by the black dash lines, respectively.

As can be observed for both cases, they follow a similar trend as described for melt C1, i.e., with a decreasing cooling rate, or allowing more time for solidification, the solidified phase fraction approaches the equilibrium value. However, the influence of the increasing cooling rate is most dominant for melt C3, followed by that of melt C2 and C1. For the cooling rates of 2 Kmin^{-1} and 10 Kmin^{-1}, for both melts C2 and C3, the solidification could reach above 90% of the equilibrium value. As can be observed from Figure 3c, even for the highest investigated cooling rate of 100 Kmin^{-1}, solidification for melt C2 could still reach 79% of the equilibrium value. However, a significant deviation from the equilibrium value could be observed for melt C3 for higher cooling rates, as has been depicted in Figure 3d. As the cooling rate increased from 40 Kmin^{-1} to 60 Kmin^{-1} to 100 Kmin^{-1}, the solid-phase fraction decreased from 69% to 48.8% to 46.3% of the equilibrium value.

3.2. Further Investigation of the Melt Conditions and the Solidification Forces Prevalent for Melts C1 and C3 for the Cooling Rates 2 Kmin^{-1} and 100 Kmin^{-1}

Melt C1, as was illustrated in the previous section, exhibited the least influence of varying cooling rates on solidification. On the other hand, the higher cooling rates significantly decreased solidification for melt C3. Hence, the melt conditions for C1 and C3 are further investigated for the lowest and the highest cooling rates of 2 Kmin^{-1} and 100 Kmin^{-1}.

Figure 4a represents the evolution of the composition field of Al_2O_3 for melt C1 at different instances of solidification for the cooling rate 2 Kmin^{-1}. At the liquidus temperature, 2030 K [60], there is no solidified fraction, and the melt composition, represented by the solid black line, is spatially homogeneous. The next stage is represented by the brown dash line when the boundary temperature has reached 1950 K. The vertical brown line represents the position of the solid/liquid interface, and the melt composition is represented by the horizontal brown dash line. It can be observed that even after considerable solidification of the stoichiometric compound γ-$LiAlO_2$, with the mole fraction of 0.5 Al_2O_3, the composition distribution of the remaining melt is nearly homogeneous. Following this, for different instances, when the system boundary temperature reached 1880 K, 1840 K, 1805 K, and finally 1750 K, similar observations could be made from the corresponding composition profiles represented by the blue solid, green dash, red solid, and olive dash lines. In Figure 4b, for all the mentioned conditions of the left boundary temperatures, the temperature and composition conditions of the solid/liquid interface have been represented by the corresponding colored boxes. As can be observed for all the cases, the interface is at equilibrium conditions, which has been represented by the black solid line. It may also be observed that the interface, which is at a considerable distance from the left boundary by the time it reaches 1750 K, is approximately at the same temperature as the left boundary. This indicates that temperature distribution was homogeneous during the solidification process for the cooling rate 2 Kmin^{-1} for the particular system dimension that was used in the simulation.

A similar representation of the melt composition distribution and the interface conditions for melt C3 are represented in Figure 4c,d for the cooling rate 2 Kmin^{-1}. Only the temperatures 2030 K and 1950 K are excluded, as the melt cooling for this case starts from its liquidus temperature, which is at 1880 K [60]. As can be observed from Figure 4c, the melt attains nearly homogeneous composition distributions in all instances. Correspondingly, the interface, as depicted in Figure 4d, is at equilibrium conditions, represented by the black solid line.

For the cooling rate of 100 Kmin^{-1}, the melt composition distribution and interface conditions for the same conditions of left boundary temperature are represented in Figure 5a,b for melt C1 and Figure 5c,d for melt C3. To understand the significant influence that this cooling rate had on suppressing the equilibrium-phase fraction formation (on C3), the different cases are further marked with their associated formed solid-phase fraction, represented in terms of the fraction of the equilibrium amounts corresponding to C1 and C3. As can be observed from Figure 5a, three further instances represented by the black, blue, and red dash lines are further included for melt C1. These represent the conditions when the solidification reached 9%, 22%, and 46% of its equilibrium value, such that a direct comparison could be made with the melt C3, and the higher influence of cooling rate on C3 compared to C1 could be further understood.

Figure 5a shows that heterogeneity in the composition field for the melt starts to evolve for melt C1 as solidification progresses. The region near the interface becomes leaner in Al_2O_3 faster than in bulk. This is observed to continue until the system reaches ~72% of its equilibrium value (system boundary at 1880 K). Following this, the melt composition tends to homogenize as the left boundary is cooled to 1750 K.

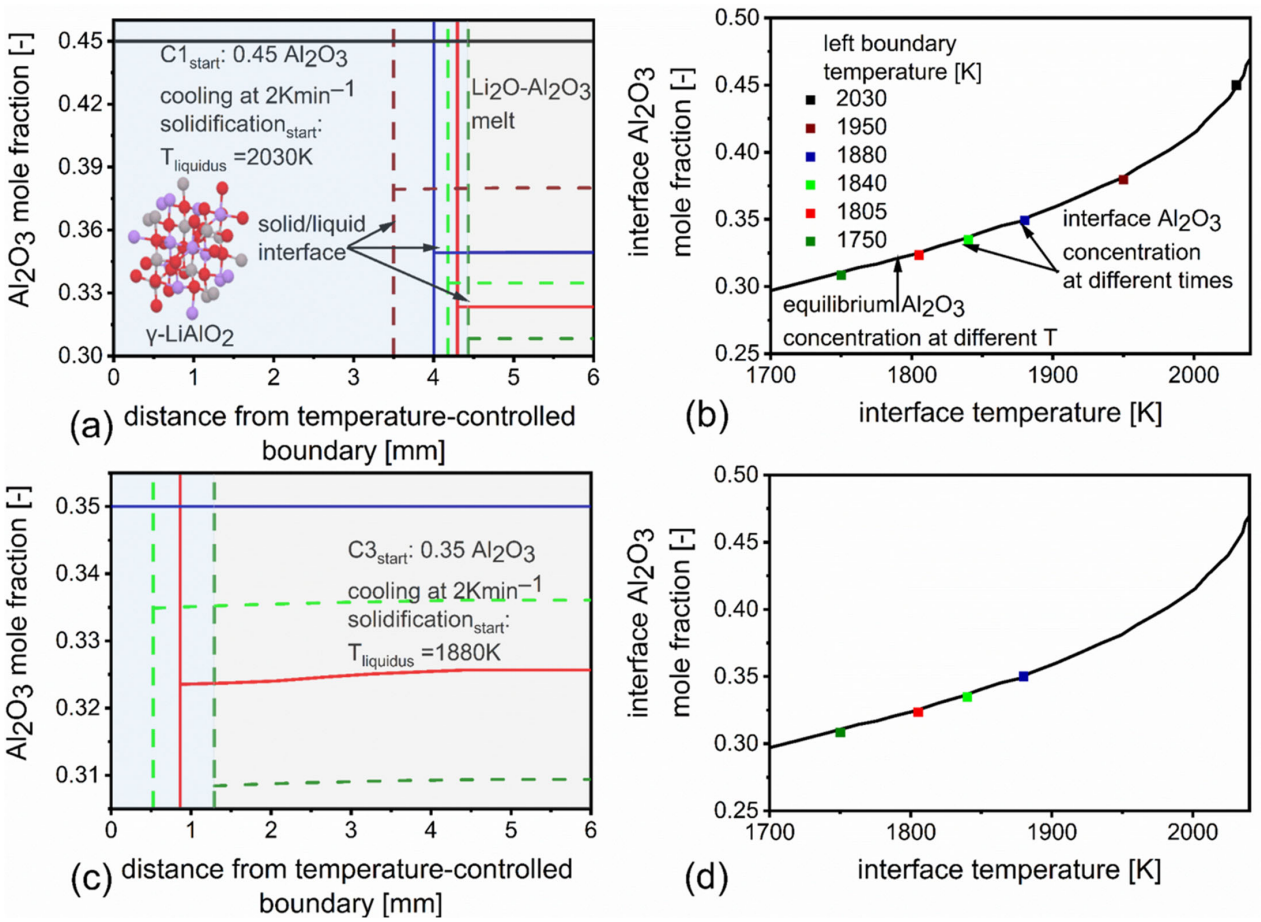

Figure 4. (**a**) Composition distribution in terms of Al_2O_3 mole fraction for the solidifying C1 melt, represented by the solid black, dash brown, solid blue, dash green, solid red, and dash olive lines for the instances when the left boundary temperature reached 2030 K, 1950 K, 1880 K, 1840 K, 1805 K, and 1750 K, respectively, for the cooling rate of 2 $Kmin^{-1}$; (**b**) equilibrium melt composition as function of temperature for melt C1 represented by the black solid line [60]; the colored boxes represent the simulated interface conditions for the corresponding instances; (**c**) similar representation as (**a**) for melt C3 for the cooling rate of 2 $Kmin^{-1}$; the calculations for 2030 K and 1950 K are excluded; (**d**) equilibrium melt composition as function of temperature for melt C3 represented by the black solid line [60]; the colored boxes represent the simulated interface conditions for the corresponding cases.

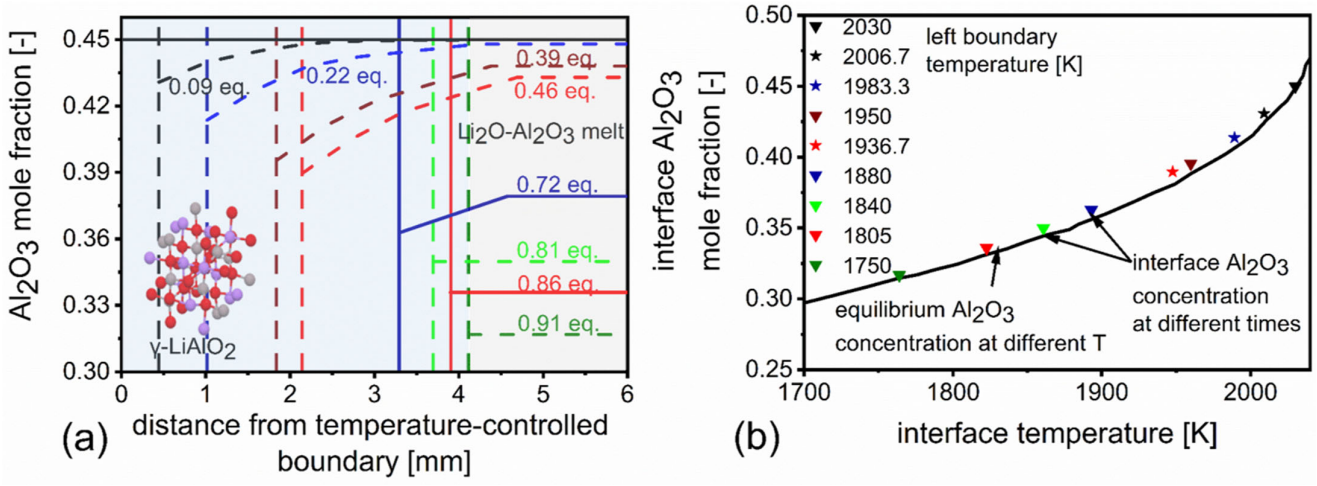

Figure 5. *Cont.*

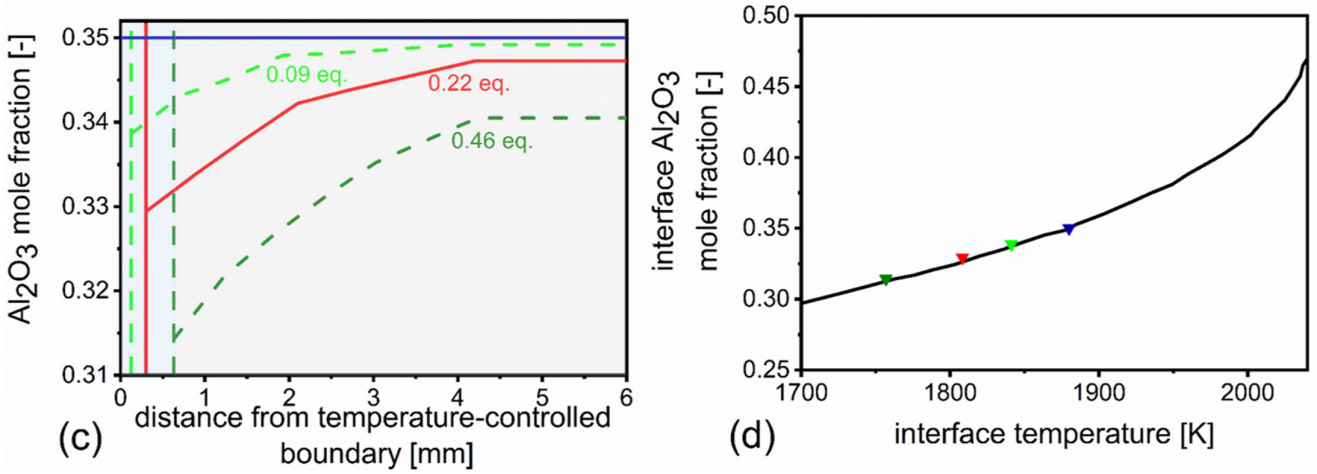

Figure 5. (**a**) Composition distribution in terms of Al_2O_3 mole fraction for the solidifying C1 melt (0.45 Al_2O_3, liquidus temperature at 2030 K), represented by the solid black, dash black, dash blue, dash brown, dash red, solid blue, dash green, solid red, and dash olive lines for the instances when the left boundary temperature reached 2030 K, 2006.7 K, 1983.3 K, 1950 K, 1936.7 K, 1880 K, 1840 K, 1805 K, and 1750 K, respectively, for the cooling rate of 100 $Kmin^{-1}$; (**b**) equilibrium melt composition as function of temperature for melt C1 represented by the black solid line [60]; the colored boxes represent the simulated interface conditions for the corresponding conditions; (**c**) similar representation as a) for melt C3 (0.35 Al_2O_3, liquidus temperature at 1880 K) for the cooling rate of 100 $Kmin^{-1}$; the calculations start from 1880 K; (**d**) equilibrium melt composition as function of temperature for melt C3 represented by the black solid line [60]; the colored boxes represent the simulated interface conditions for the corresponding cases.

The interface is at equilibrium conditions for most of the melt, as can be observed from Figure 5b. However, between temperatures 2030 K and 1880 K, a minor deviation from the equilibrium condition is observed for the interface. Additionally, the interface temperature (consequently, the rest of the melt) shows considerable deviation from the left boundary temperature.

For the fast cooling rate of 100 $Kmin^{-1}$, the evolution of the significant heterogeneity for the melt composition distribution is represented in Figure 5c for similar instances as in Figure 4c. The corresponding solid amount in terms of the fraction of the equilibrium amount is depicted for these instances. Figure 5d further illustrates the interface conditions for melt C3. As can be observed, the interfaces attain the equilibrium condition for each instance during the solidification process.

3.3. Evolution of the Temperature Field for Melts C1 and C3 for the Cooling Rate 100 $Kmin^{-1}$

Investigating the evolution of the temperature field in combination with the concentration field might be necessary to illustrate the difference in the influence of the fast cooling rate of 100 $Kmin^{-1}$ on the solidification of melt C1 as compared to melt C3. Figure 6a,b represents the simulated temperature fields for melts C1 and C3 at the same instances for which the composition fields were depicted in Figure 5a,c. The three cases for which solidification for both C1 and C3 reaches 9%, 22%, and 46% of their corresponding equilibrium values are further marked in Figure 6a,b. The deviation of the bulk melt temperature from the left boundary temperature is observed to be much smaller for C1 as compared to C3 at the end of the cooling process (left boundary at 1750 K).

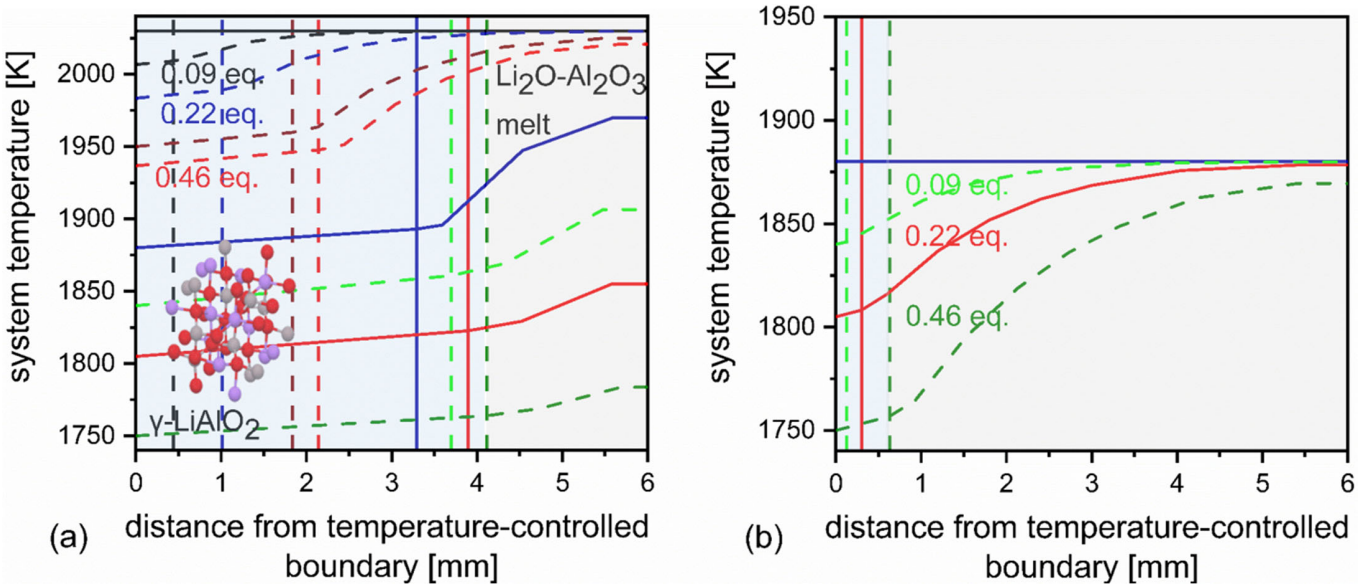

Figure 6. (**a**) Temperature distribution for the solidifying C1 melt, represented by the solid black, dash black, dash blue, dash brown, dash red, solid blue, dash green, solid red, and dash olive lines for the instances when the left boundary temperature reached 2030 K, 2006.7 K, 1983.3 K, 1950 K, 1936.7 K, 1880 K, 1840 K, 1805 K, and 1750 K, respectively, for the cooling rate of 100 $Kmin^{-1}$; (**b**) similar representation as (**a**) for melt C3 for the cooling rate of 100 $Kmin^{-1}$; the calculations start from 1880 K; the corresponding solidified phase amount as a fraction of the equilibrium amount is presented.

3.4. Investigation for the Solidification Evolution for Melt C3 When the Boundary Temperature Is Held Constant at 1750 K for 20 Min Following the Cooling Regime from 1880 K to 1750 K at 100 $Kmin^{-1}$

Cooling melt C3 at 100 $Kmin^{-1}$ results in a significant deviation from the equilibrium amount, as depicted in Figure 3d. To investigate whether the system can reach its equilibrium condition at 1750 K when enough evolution time is provided, the left boundary temperature is held constant at 1750 K for 20 min following the cooling regime.

The evolution of the left system boundary temperature with time is represented by the solid black line in Figure 7a. The corresponding solid fraction evolution is represented by the solid blue line. The equilibrium fraction corresponding to melt C3 at temperature 1750 K is represented by the dash blue line. Five time instances, t_1 to t_5, are marked by the olive dash line, brown solid line, green dash line, red solid line, and blue dash line, respectively. t_1 represents the time when the left boundary temperature reaches 1750 K. Following this, an interval of 60 s each is observed to reach from t_1 to t_4. t_5 represents the end of the simulation regime. For the time steps t_1 to t_5, the evolution of the melt composition is represented by the corresponding lines in Figure 7b. The corresponding solid amount as a fraction of the equilibrium amount is also represented. As can be observed from Figure 7b, within the first 180 s of the total 20 min holding period, the solid fraction increased from 46% to 90%. During the remaining time, the solidification increased further to 96%.

Hence, it might be concluded that most of the solid-phase evolution occurred within the first 180 s of the holding period, after which the solidification rate decreased significantly, as can also be observed in Figure 7b. The temperature evolution of the system for these time instances, represented in Figure 7c, depicts the gradual homogenization of the temperature field over time.

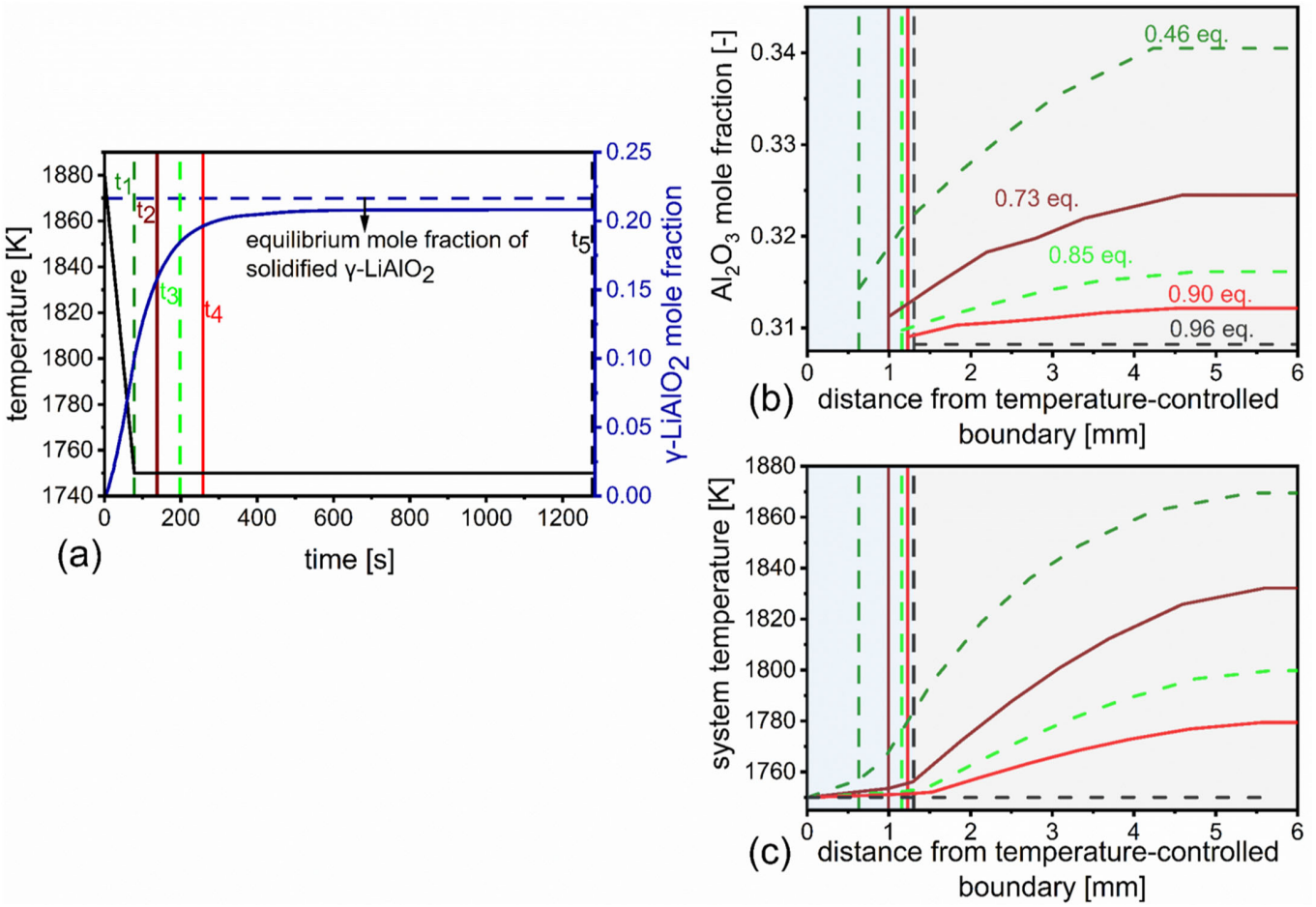

Figure 7. (**a**) Left boundary temperature over time represented by the black solid line for a cooling melt C3 from 1880 K to 1750 K at 100 $Kmin^{-1}$, followed by a holding period of 20 min; solid fraction evolution for the same duration represented by blue solid line; equilibrium solid fraction for melt C3 at 1750 K; different time instances, t_1, t_2, t_3, t_4, and t_5 are represented by the olive dash, brown solid, green dash, red solid and blue dash lines, respectively; (**b**) composition distribution in terms of Al_2O_3 mole fraction for the solidifying C3 melt, represented for the time steps t_1, t_2, t_3, t_4, and t_5; the corresponding generated solid amount as a fraction of the equilibrium amount is presented; (**c**) temperature distribution for the solidifying C3 melt, represented for the time instances t_1, t_2, t_3, t_4, and t_5.

4. Discussion

In this work, the solidification of γ-$LiAlO_2$ has been studied from a binary melt of Li_2O-Al_2O_3 and its dependence on external cooling rates and initial melt compositions. It could be observed from the results represented in Figure 3b–d that for lower cooling rates, like 2 $Kmin^{-1}$ and 10 $Kmin^{-1}$, for all the melts (C1, C2, C3), the solidification could reach a near-equilibrium value. The governing factors for solidification under a low cooling rate (2 $Kmin^{-1}$) might be understood from the melt condition investigation for C1 and C3, represented in Figure 4a–d.

For the solidification of a 0.5 mole fraction Al_2O_3 stoichiometric compound from a melt that is leaner in Al_2O_3, the bulk melt composition needs to decrease further in terms of Al_2O_3 mole fraction in order to generate the solid phase with the higher amount of Al_2O_3. For any temperature lower than the liquidus for a certain composition, the simultaneous generation of a certain amount of solid phase from the melt, i.e., the interface migration and the reduction of the composition of the remaining melt that necessitates diffusion, might be time-consuming. Hence, either the external cooling has to be very slow to allow the system to equilibrate, or the internal kinetics of interface mobility and component

and thermal diffusion have to be very fast to observe for any temperature a solidification evolution that is in accordance with that of the equilibrium studies. For the cooling rate of 2 $Kmin^{-1}$, which is much higher than what has been used in the literature for the experimental determination of equilibrium solidification [23,27], for both melts C1 and C3, the internal kinetics are still fast enough to reach near-equilibrium status for any of the instances studied. This is further illustrated by the almost homogeneous composition fields of the melts and the equilibrium interface conditions for each instance investigated. Such fast solidification kinetics for γ-$LiAlO_2$ have also been experimentally observed for systems having compositions close to the stoichiometric compound in [60].

Increasing the external cooling rate to 100 $Kmin^{-1}$ signified fifty times less duration for solidification than the former case. Because of this short span of time, only the melt in the vicinity of the interface reaches the equilibrium composition value for that temperature. The rest of the bulk melt still remains at a higher Al_2O_3 concentration value. Thus, due to the dearth of supply of Al_2O_3 at the interface, the solid fractions formed are less than the equilibrium phase fraction value. However, it is interesting to note that this effect is more pronounced for melt C3 than for melt C1.

Figure 5c,d depicts that melt C3 takes a duration of 78 s, which is the time taken for cooling the left boundary temperature from 1880 K to 1750 K to reach 46% of its equilibrium fraction. However, for the same cooling rate of 100 $Kmin^{-1}$, it can be observed from Figure 5a,b that melt C1 reaches 46% of its equilibrium value when the left boundary temperature cools down to 1936.7 K from 2030 K; i.e., in ~56 s. Thus, overall, more solidified fraction is generated in the case of C1 (as can be compared from Figure 5a,c) in a lesser time than that of C2 as both the systems reach 46% of their equilibrium growth. This might be explained by the fact that as the composition of C1 (0.45 mole fraction Al_2O_3) is closer to the stoichiometric compound (0.5 mole fraction Al_2O_3) as compared to C3, less diffusion is required in order to generate the same amount of solid phase for C1 than C3. Moreover, it can also be observed from the temperature profiles of C1 and C3, represented in Figure 6a,b, that the overall system temperature for any instant, as melt C1 progressively generates 9%, 22%, and 46% of the equilibrium solid fraction, is at a higher level than when melt C3 generates the corresponding amounts of solids. This implies that diffusion kinetics were faster for these instances for C1 than for C3, and, hence, solidification was faster for the former case.

The solidification of melts C1 and C3 might also be compared from the cases when for both the systems the left boundary temperature reaches 1880 K (the liquidus temperature for C3) and progressively decreases to 1840 K-1805 K-1750 K. As can be observed from Figure 5a,c, at the instant solidification starts for C3 (at 1880 K), melt C1 has already reached a solidification corresponding to 72% of its equilibrium value. The overall melt composition has reduced much from its initial composition (0.45 Al_2O_3) for C1. For the subsequent time steps, as the temperature drops, the composition of melt C1 nears that of melt C3, requiring more diffusion for the solidification of γ-$LiAlO_2$ than what was required before when the melt composition was nearer to the solid-phase composition. However, as can be compared between Figure 5a,c, the distance for diffusion is much reduced for melt C1, which already has a considerable fraction of the solid formed, compared to melt C3. Hence, even though the overall melt composition of C1 approaches that of C3 and goes even lower than C3 after a certain instant, the diffusion is quick enough for the solidification of C1 to reach up to 91% of its equilibrium value. On the other hand, the much larger distance for diffusion suppresses the solidification for C3 at 46%.

The faster diffusion kinetics of melt C3 compared to melt C1, as can be comprehended from the higher level of bulk melt temperature for the former for the instances where the boundary temperatures reached 1840 K-1805 K-1750 K, which is depicted in Figure 6a,b, compensated for the larger diffusion distances in C3 and were just enough to generate an equivalent amount of solid for C3, as was generated for melt C1 for this particular duration.

It must be mentioned here that, since for most of the cases investigated for melts C1 and C3 for the cooling rates of 2 $Kmin^{-1}$ and 100 $Kmin^{-1}$, the interface was observed to be

at equilibrium conditions, as denoted in Figure 4b,d and Figure 5b,d, the assumption that solidification might be considered to be diffusion-limited for the cases of very high cooling rates (~60 $Kmin^{-1}$ or 100 $Kmin^{-1}$) is substantiated.

The faster homogenizing thermal profiles for the instances 1840 K-1805 K-1750 K for melt C1 as compared to C3 could be attributed to the fact that the larger fraction of solid, with a higher thermal diffusivity than the melt, provides a quicker way for heat extraction for the former.

Finally, for melt C3, the results depicted in Figure 7 show that, in the absence of a dynamic cooling rate, if the external heat extraction profile is just enough to hold the temperature at 1750 K, the solidification reaches 90% of its equilibrium value as fast as within a 180 s duration. The system temperature also quickly equilibrates. This signifies the inherent fast kinetics of the Li_2O-Al_2O_3 system, especially for the solidification of γ-$LiAlO_2$.

5. Conclusions

This work presents a strategy for coupling MD simulation information and a recently developed new CALPHAD database to the kinetic TEP model that facilitates the study of solidification kinetics from slag melts under non-equilibrium heat extraction strategies for γ-$LiAlO_2$. The modeling strategy based on Gibbs energy dissipation during solidification could be facilitated by the dynamic input of the available Gibbs energies for the system under any given condition by the CALPHAD database at each temporal level of evolution. The TEP framework is applied in this work such that its constituting kinetic parameters, i.e., diffusion coefficients, are obtained computationally based on MD.

The MD-informed TEP model is applied in this work to investigate the solidification kinetics of γ-$LiAlO_2$ out of the binary Li_2O-Al_2O_3 melt. It turned out that for initial compositions in the melt near the stoichiometric compound composition, even a cooling rate as high as 100 $Kmin^{-1}$ does not influence the generation of the equilibrium phase amount significantly. This signifies that for a certain composition range in the vicinity of the stoichiometric composition, the kinetics of diffusion have a negligible influence on the γ-$LiAlO_2$ formation. This supports observations already made for γ-$LiAlO_2$ phase formation for other melt systems [75]. However, with increasing deviation of the initial melt composition from that of the stoichiometric compound, it could be observed that irrespective of the fast reaction kinetics for the formation of the compound itself, the diffusion required to form the precursor composition in the melt for the solidification to occur becomes increasingly significant. Consequently, time-dependent cooling strategies trigger non-equilibrium phase fractions in the binary Li_2O-Al_2O_3 melt and help us to understand the transition from thermodynamic and kinetic-driven phase transitions.

Author Contributions: Conceptualization, S.C. and M.F.; methodology, S.C., M.F., D.A.D.A., O.F., I.A.A., N.M., A.S., T.S. and U.E.A.F.; investigation, S.C. and M.F.; writing—original draft preparation, S.C.; writing—review and editing, S.C., M.F., D.A.D.A., O.F., I.A.A., N.M., A.S., T.S. and U.E.A.F.; supervision, M.F., O.F., N.M., T.S. and U.E.A.F.; funding acquisition, M.F. All authors have read and agreed to the published version of the manuscript.

Funding: This research was funded by the Deutsche Forschungsgemeinschaft (DFG, German Research Foundation) in the priority program 2315 "Engineered artificial minerals (EnAM)—A geo-metallurgical tool to recycle critical elements from waste streams" with grant number 470323858, 470367641, 470392360, 470309740.

Data Availability Statement: The data presented in this study are available upon request from the corresponding author.

Acknowledgments: We acknowledge the support of the Open Access Publishing Fund of Clausthal University of Technology.

Conflicts of Interest: The authors declare that they have no known competing financial interests or personal relationships that could have appeared to influence the work reported in this paper.

References

1. Hayes, P.C.; Nicol, S.; Jak, E. Solidification of oxide melts. In Proceedings of the 11th International Conference on Molten Slags, Fluxes and Salts, E-Proceedings, EA20191127–0704, Virtual, Seoul, Republic of Korea, 21–25 February 2021.
2. Tian, Y.; Li, G.; Li, Y.; Li, T.; Yuan, C.; Liu, Y. Thermodynamics and Kinetics on Hot State Modification of BOF Slag by Adding SiO_2. *Metall. Mater. Trans. B* **2023**, *54*, 1131–1143. [CrossRef]
3. Wang, Z.; Sohn, I. Understanding the solidification and leaching behavior of synthesized Cr-containing stainless steel slags with varying Al_2O_3/SiO_2 mass ratios. *Ceram. Int.* **2021**, *47*, 10918–10926. [CrossRef]
4. Ding, B.; Liao, Q.; Zhu, X.; Wang, H. Deep insight into phase transition and crystallization of high temperature molten slag during cooling: A review. *Appl. Therm. Eng.* **2021**, *184*, 116260. [CrossRef]
5. Esfahani, S.; Barati, M. Effect of slag composition on the crystallization of synthetic CaO–SiO_2–Al_2O_3–MgO slags: Part I—Crystallization behavior. *J. Non-Cryst. Solids* **2016**, *436*, 35–43. [CrossRef]
6. Zeng, Q.; Li, J.; Yu, Y.; Zhu, H. Effect of Cooling Rate on Crystallization Behavior of CaO-SiO_2-MgO-Cr_2O_3 Based Slag. *High Temp. Mat. Process.* **2020**, *39*, 74–80. [CrossRef]
7. Gan, L.; Zhang, C.; Zhou, J.; Shangguan, F. Continuous cooling crystallization kinetics of a molten blast furnace slag. *J. Non-Cryst. Solids* **2012**, *358*, 20–24. [CrossRef]
8. Klaffenbach, E.; Montenegro, V.; Guo, M.; Blanpain, B. Sustainable and comprehensive utilization of copper slag: A review and critical analysis. *J. Sustain. Met.* **2023**, *9*, 468–496. [CrossRef]
9. Wang, Z.; Sohn, I. Selective elemental concentration during the solidification of stainless steel slags for increased Cr recovery with MnO addition. *J. Am. Ceram. Soc.* **2020**, *103*, 6012–6024. [CrossRef]
10. Huo, X.; Zhang, X.; Ding, Z.; Zhang, M.; Guo, M. A clean approach for detoxification of industrial chromium-bearing stainless steel slag: Selective crystallization control and binary basicity effect. *J. Hazard. Mater.* **2023**, *446*, 130746. [CrossRef]
11. Li, Y.; Gao, J.; Lan, X.; Feng, G.; Zhang, Y.; Guo, Z. Solidification and recovery of Cr from hazardous Cr-bearing steel slag: Selective solidification, super-gravity separation and crystal characterization. *Sep. Purif. Technol.* **2023**, *306*, 122616. [CrossRef]
12. Wittkowski, A.; Schirmer, T.; Qiu, H.; Goldmann, D.; Fittschen, U.E. Speciation of manganese in a synthetic recycling slag relevant for lithium recycling from lithium-ion batteries. *Metals* **2021**, *11*, 188. [CrossRef]
13. Schirmer, T.; Qiu, H.; Goldmann, D.; Stallmeister, C.; Friedrich, B. Influence of P and Ti on Phase Formation at Solidification of Synthetic Slag Containing Li, Zr, La, and Ta. *Minerals* **2022**, *12*, 310. [CrossRef]
14. Das, P.; Upadhyay, S.; Dubey, S.; Singh, K.K. Waste to wealth: Recovery of value-added products from steel slag. *J. Environ. Chem. Eng.* **2021**, *9*, 105640. [CrossRef]
15. Schirmer, T.; Hiller, J.; Weiss, J.; Munchen, D.; Lucas, H.; Fittschen, U.E.; Friedrich, B. Behavior of Tantalum in a Fe-Dominated Synthetic Fayalitic Slag System—Phase Analysis and Incorporation. *Minerals* **2024**, *14*, 262. [CrossRef]
16. Ma, Z.; Zhao, Z.; Guo, W.; Guo, X. Effect of TiO_2 Addition and Cooling Rate on Crystallization Behavior of Separated Slag Containing Low-grade RE. *ISIJ Int.* **2023**, *63*, 1274–1280. [CrossRef]
17. Li, Z.; Li, J.; Sun, Y.; Seetharaman, S.; Liu, L.; Wang, X.; Zhang, Z. Effect of Al 2 O 3 addition on the precipitated phase transformation in Ti-bearing blast furnace slags. *Metall. Mater. Trans. B* **2016**, *47*, 1390–1399. [CrossRef]
18. Liu, L.; Hu, M.L.; Bai, C.G.; Lü, X.W.; Xu, Y.Z.; Deng, Q.Y. Effect of cooling rate on the crystallization behavior of perovskite in high titanium-bearing blast furnace slag. *Int. J. Min. Met. Mater.* **2014**, *21*, 1052–1061. [CrossRef]
19. Li, B.; Du, X.; Shen, Y.; Zhang, Z.; Rong, T. Nonisothermal crystallization, growth, and shape control of magnetite crystals in molten nickel slag during continuous cooling. *Metall. Mater. Trans. B* **2022**, *53*, 1816–1826. [CrossRef]
20. Huang, Z.; Qiu, R.; Lin, K.; Ruan, J.; Xu, Z. In situ recombination of elements in spent lithium-ion batteries to recover high-value γ-$LiAlO_2$ and $LiAl_5O_8$. *Environ. Sci. Tech.* **2021**, *55*, 7643–7653. [CrossRef]
21. Lourens, F.; Suhr, E.; Schnickmann, A.; Schirmer, T.; Ludwig, A. High-Throughput Study of the Phase Constitution of the Thin Film System Mg-Mn-Al-O. Adv. *Eng. Mater.* **2024**, *26*, 2302091.
22. Schwan, L.; Bröckel, U. First Approach Using Fluidic Force Microscopy (FluidFM®) to Measure Adhesion Forces between Droplets and Flat/Rough Surfaces Immersed in Water. *Processes* **2024**, *12*, 99. [CrossRef]
23. Schnickmann, A.; Hampel, S.; Schirmer, T.; Fittschen, U.E. Formation of Lithium-Manganates in a Complex Slag System Consisting of Li_2O-MgO-Al_2O_3-SiO_2-CaO-MnO—A First Survey. *Metals* **2023**, *13*, 2006. [CrossRef]
24. Acker, S.; Namyslo, J.C.; Rudolph, M.; Strube, F.; Fittschen, U.E.; Qiu, H.; Goldmann, D.; Schmidt, A. Polyether-tethered imidazole-2-thiones, imidazole-2-selenones and imidazolium salts as collectors for the flotation of lithium aluminate and spodumene. *RSC Adv.* **2023**, *13*, 6593–6605. [CrossRef] [PubMed]
25. Zgheib, A.; Acker, S.; Fischer, M.H.; Namyslo, J.C.; Strube, F.; Rudolph, M.; Fittschen, U.E.A.; Wollmann, A.; Weber, A.P.; Nieger, M.; et al. Lithium aluminate flotation by pH-and light-switchable collectors based on the natural product punicine. *RSC Adv.* **2024**, *14*, 9353–9364. [CrossRef] [PubMed]
26. Li, H.; Ranneberg, M.; Fischlschweiger, M. High-Temperature Phase Behavior of Li_2O-MnO with a Focus on the Liquid-to-Solid Transition. *JOM* **2023**, *75*, 5796–5807. [CrossRef]
27. Schnickmann, A.; De Abreu, D.A.; Fabrichnaya, O.; Schirmer, T. Stabilization of Mn4+ in synthetic slags and identification of important slag forming phases. *Minerals* **2024**, *14*, 368. [CrossRef]
28. Li, H.; Qiu, H.; Schirmer, T.; Goldmann, D.; Fischlschweiger, M. Tailoring Lithium Aluminate Phases Based on Thermodynamics for an Increased Recycling Efficiency of Li-Ion Batteries. *ACS ES T Eng.* **2022**, *2*, 1883–1895. [CrossRef]

29. Dolotko, O.; Gehrke, N.; Malliaridou, T.; Sieweck, R.; Herrmann, L.; Hunzinger, B.; Knapp, M.; Ehrenberg, H. Universal and efficient extraction of lithium for lithium-ion battery recycling using mechanochemistry. *Commun. Chem.* **2023**, *6*, 49. [CrossRef]
30. Schirmer, T.; Wahl, M.; Bock, W.; Kopnarski, M. Determination of the Li distribution in synthetic recycling slag with SIMS. *Metals* **2021**, *11*, 825. [CrossRef]
31. Elwert, T.; Goldmann, D.; Strauss, K.; Schirmer, T. Phase composition of high lithium slags from the recycling of lithium ion batteries. *World Metall. Erzmetall* **2012**, *65*, 163–171.
32. Tabero, P.; Frąckowiak, A.; Dąbrowska, G. Reinvestigations of the LiO–AlO system. Part I: LiAlO and LiAlO. *Polish J. Chem. Technol.* **2021**, *23*, 30–36.
33. Qiu, H.; Li, H.; Fischlschweiger, M.; Ranneberg, M.; Graupner, T.; Lucas, H.; Stallmeister, C.; Friedrich, B.; Yagmurlu, B.; Goldmann, D. Valorization of lithium containing slags from pyrometallurgical recycling route of spent lithium-ion batteries: The enrichment of γ-$LiAlO_2$ phase from thermodynamic controlled and modified slags. *Miner. Eng.* **2024**, *217*, 108918. [CrossRef]
34. Setyawan, W.; Senor, D.J.; Devanathan, R. Role of interfaces in damage process of irradiated lithium aluminate nanocrystals. *J. Am. Ceram. Soc.* **2019**, *102*, 1982–1993. [CrossRef]
35. Twardak, A.; Bilski, P.; Marczewska, B.; Lee, J.I.; Kim, J.L.; Gieszczyk, W.; Mrozik, A.; Sądel, M.; Wróbel, D. Properties of lithium aluminate for application as an OSL dosimeter. *Radiat. Phys. Chem.* **2014**, *104*, 76–79. [CrossRef]
36. Abdou, M.A.; Morley, N.B.; Ying, A.Y. Overview of fusion blanket R&D in the US over the last decade. *Nucl. Eng. Technol.* **2005**, *37*, 401–422.
37. Terada, S.; Nagashima, I.; Higaki, K.; Ito, Y. Stability of $LiAlO_2$ as electrolyte matrix for molten carbonate fuel cells. *J. Power Sources* **1998**, *75*, 223–229. [CrossRef]
38. Schirmer, T.; Qiu, H.; Li, H.; Goldmann, D.; Fischlschweiger, M. Li-distribution in compounds of the Li_2O-MgO-Al_2O_3-SiO_2-CaO system—A first survey. *Metals* **2020**, *10*, 1633. [CrossRef]
39. Rannenberg, M.; Lucas, H.; Li, H.; Graupner, T.; Fischlschweiger, M.; Friedrich, B. Evaluation of Li and Mn influence on Al-Ca-Si-O slag system regarding pyrometallurgical LIB treatment. In Proceedings of the 8th International Slag Valorisation Symposium, Leuven, Belgium, 18–20 April 2023; pp. 205–209.
40. Sommerfeld, M.; Vonderstein, C.; Dertmann, C.; Klimko, J.; Oráč, D.; Miškufová, A.; Havlík, T.; Friedrich, B. A combined pyro-and hydrometallurgical approach to recycle pyrolyzed lithium-ion battery black mass part 1: Production of lithium concentrates in an electric arc furnace. *Metals* **2020**, *10*, 1069. [CrossRef]
41. Li, Y.; Guo, K.; Xiang, J.; Pei, G.; Lv, X. Effect of cooling method on the mineralogy and stability of steel slag. *ISIJ Int.* **2022**, *62*, 2197–2206. [CrossRef]
42. Liu, J.J.; Chen, G.; Yan, P.C.; Planpain, B.; Moelans, N.; Guo, M. In-situ observation of isothermal $CaSiO_3$ crystallization in CaO–Al_2O_3–SiO_2 melts: A study of the effects of temperature and composition. *J. Cryst. Growth* **2014**, *402*, 1–8. [CrossRef]
43. Klug, J.L.; Hagemann, R.; Heck, N.C.; Vilela, A.C.; Heller, H.P.; Scheller, P.R. Solidification Behaviour of Slags: The Single Hot Thermocouple Technique. *J. Manuf. Sci. Prod.* **2013**, *13*, 91–102. [CrossRef]
44. Rachmawati, C.; Weiss, J.; Lucas, H.I.; Löwer, E.; Leißner, T.; Ebert, D.; Möckel, R.; Friedrich, B.; Peuker, U.A. Characterisation of the Grain Morphology of Artificial Minerals (EnAMs) in Lithium Slags by Correlating Multi-Dimensional 2D and 3D Methods. *Minerals* **2024**, *14*, 130. [CrossRef]
45. Chakrabarty, S.; Li, H.; Schirmer, T.; Hampel, S.; Fittschen, U.E.; Fischlschweiger, M. Non-equilibrium thermodynamic modelling of cooling path dependent phase evolution of Li_2SiO_3 from Li_2O-SiO_2 melt by considering mixed kinetic phenomena and time-dependent concentration fields. *Scr. Mater.* **2024**, *242*, 115922. [CrossRef]
46. Nicol, S.; Jak, E.; Hayes, P.C. Effect of the CaO/SiO_2 ratio on the controlled solidification of 'Fe2O3'-CaO-SiO2 melts in air. *Min. Proc. Extr. Met. Rev.* **2022**, *131*, 99–110. [CrossRef]
47. Diao, J.; Xie, B.; Wang, Y.; Ji, C.Q. Mineralogical characterisation of vanadium slag under different treatment conditions. *Ironmak. Steelmak.* **2009**, *36*, 476–480. [CrossRef]
48. Esfahani, S.; Barati, M. Purification of metallurgical silicon using iron as an impurity getter part I: Growth and separation of Si. *Met. Mater. Int.* **2011**, *17*, 823–829. [CrossRef]
49. Durinck, D.; Jones, P.T.; Blanpain, B.; Wollants, P.; Mertens, G.; Elsen, J. Slag solidification modeling using the Scheil–Gulliver assumptions. *J. Am. Ceram. Soc.* **2007**, *90*, 1177–1185. [CrossRef]
50. Jung, S.S.; Kim, G.B.; Sohn, I. Understanding the solidification of stainless steel slag and dust mixtures. *J. Am. Ceram. Soc.* **2017**, *100*, 3771–3783. [CrossRef]
51. Svoboda, J.; Turek, I.; Fischer, F.D. Application of the thermodynamic extremal principle to modeling of thermodynamic processes in material sciences. *Phil. Mag.* **2005**, *85*, 3699–3707. [CrossRef]
52. Fischer, F.D.; Svoboda, J.; Petryk, H. Thermodynamic extremal principles for irreversible processes in materials science. *Acta Mater.* **2014**, *67*, 1–20. [CrossRef]
53. Svoboda, J.; Vala, J.; Gamsjäger, E.; Fischer, F.D. A thick-interface model for diffusive and massive phase transformation in substitutional alloys. *Acta Mater.* **2006**, *54*, 3953–3960. [CrossRef]
54. Svoboda, J.; Fischer, F.D.; Fratzl, P. Diffusion and creep in multi-component alloys with non-ideal sources and sinks for vacancies. *Acta Mater.* **2006**, *54*, 3043–3053. [CrossRef]
55. Svoboda, J.; Gamsjäger, E.; Fischer, F.D. Modeling of massive transformation in substitutional alloys. *Met. Mater. Trans. A* **2006**, *37*, 125–132. [CrossRef]

56. Abart, R.; Svoboda, J.; Jeřabek, P.; Povoden-Karadeniz, E.; Habler, G. Interlayer growth kinetics of a binary solid-solution based on the thermodynamic extremal principle: Application to the formation of spinel at periclase-corundum contacts. *Am. J. Sci.* **2016**, *316*, 309–328. [CrossRef]
57. Chakrabarty, S.; Li, H.; Fischlschweiger, M. Calphad-informed thermodynamic non-equilibrium simulation of non-isothermal solid-state reactions of magnesium aluminate spinel based on the thermodynamic extremal principle. *Materialia* **2023**, *28*, 101723. [CrossRef]
58. Chakrabarty, S.; Li, H.; Fischlschweiger, M. Control of Interface Migration in Nonequilibrium Crystallization of Li2SiO3 from Li2O–SiO2 Melt by Spatiotemporal Temperature and Concentration Fields. *ACS Omega* **2024**, *9*, 21557–21568. [CrossRef]
59. Hampel, S.; Alhafez, I.A.; Schirmer, T.; Merkert, N.; Schnickmann, A.; Li, H.; Fischlschweiger, M.; Adriane, U.E. Engineering compounds for the recovery of critical elements from slags: Melt characteristics of Li_5AlO_4, $LiAlO_2$ and $LiAl_5O_8$. *ACS Omega* **2024**, *9*, 24584–24592. [CrossRef]
60. De Abreu, D.A.; Löffler, M.; Kriegel, M.J.; Fabrichnaya, O. Experimental Investigation and Thermodynamic Modeling of the Li_2O–Al_2O_3 System. *J. Phase Equil. Diffus.* **2024**, *15*, 1–20.
61. Kurz, W.; Fisher, D.J.; Rappaz, M. *Fundamentals of Solidification*, 5th ed.; Trans Tech Publications Limited: Stafa-Zurich, Switzerland, 2023.
62. Svoboda, J.; Gamsjäger, E.; Fischer, F.D.; Fratzl, P. Application of the thermodynamic extremal principle to the diffusional phase transformations. *Acta Mater.* **2004**, *52*, 959–967. [CrossRef]
63. Jain, A.; Ong, S.P.; Hautier, G.; Chen, W.; Richards, W.D.; Dacek, S.; Cholia, S.; Gunter, D.; Skinner, D.; Ceder, G.; et al. Commentary: The Materials Project: A materials genome approach to accelerating materials innovation. *APL Mater.* **2013**, *1*, 011002. [CrossRef]
64. Hackl, K.; Fischer, F.D.; Svoboda, J. A study on the principle of maximum dissipation for coupled and non-coupled non-isothermal processes in materials. *Proc. R. Soc. A* **2011**, *467*, 1186–1196. [CrossRef]
65. Coulson, J.M.; Richardson, J.F.; Backhurst, J.R.; Harker, J.H. *Chemical Engineering: Fluid Flow, Heat Transfer and Mass Transfer*; Pergamon Press: Oxford, UK, 1990; Volume 1.
66. Denuziere, C.; Roux, N. *Data and Properties of Lithium Aluminate γ $LiAlO_2$ (No. CEA-N-2548)*; CEA Centre d'Etudes Nucleaires de Saclay: Gif-sur-Yvette, France, 1988.
67. Schulz, B.; Wedemeyer, H. Preparation, characterization and thermal diffusivity of γ-$LiAlO_2$. *J. Nucl. Mater.* **1986**, *139*, 35–41. [CrossRef]
68. Leitner, M.; Leitner, T.; Schmon, A.; Aziz, K.; Pottlacher, G. Thermophysical properties of liquid aluminum. *Met. Mater. Trans. A* **2017**, *48*, 3036–3045. [CrossRef]
69. Waseda, Y.; Ohta, H.; Shibata, H.; Nishi, T. Thermal diffusivity measurements of oxide and metallic melts at high temperature by the laser flash method. *High Temp. Mater. Process.* **2002**, *21*, 387–398. [CrossRef]
70. Lukas, H.; Fries, S.G.; Sundman, B. *Computational Thermodynamics: The Calphad Method*; Cambridge University Press: Cambridge, UK, 2007; Volume 313.
71. Chakraborty, S. Diffusion in silicate melts. *Rev. Mineral.* **1995**, *32*, 411–504.
72. Oishi, Y.; Nanba, M.; Pask, J.A. Analysis of Liquid-State Interdiffusion in the System CaO-Al_2O_3-SiO_2 Using Multiatomic Ion Models. *J. Am. Ceram. Soc.* **1982**, *65*, 247–253. [CrossRef]
73. Kuganathan, N.; Dark, J.; Sgourou, E.N.; Panayiotatos, Y.; Chroneos, A. Atomistic simulations of the defect chemistry and self-diffusion of Li-ion in $LiAlO_2$. *Energies* **2019**, *12*, 2895. [CrossRef]
74. Thompson, A.P.; Aktulga, H.M.; Berger, R.; Bolintineanu, D.S.; Brown, W.M.; Crozier, P.S.; in't Veld, P.J.; Kohlmeyer, A.; Moore, S.G.; Nguyen, T.D.; et al. LAMMPS-a flexible simulation tool for particle-based materials modeling at the atomic, meso, and continuum scales. *Comput. Phys. Commun.* **2022**, *271*, 108171. [CrossRef]
75. Li, H.; Qiu, H.; Ranneberg, M.; Lucas, H.; Graupner, T.; Friedrich, B.; Yagmurlu, B.; Goldmann, D.; Bremer, J.; Fischlschweiger, M. Enhancing Lithium Recycling Efficiency in Pyrometallurgical Processing through Thermodynamic-Based Optmization and Design of Spent Lithium-Iom Battery Slag Compositions. *ACS Sustain. Resour. Manag.* **2024**, *1*, 1170–1184. [CrossRef]